RSC Advances

This is an *Accepted Manuscript*, which has been through the Royal Society of Chemistry peer review process and has been accepted for publication.

Accepted Manuscripts are published online shortly after acceptance, before technical editing, formatting and proof reading. Using this free service, authors can make their results available to the community, in citable form, before we publish the edited article. This *Accepted Manuscript* will be replaced by the edited, formatted and paginated article as soon as this is available.

You can find more information about *Accepted Manuscripts* in the Information for Authors.

Please note that technical editing may introduce minor changes to the text and/or graphics, which may alter content. The journal's standard Terms & Conditions and the Ethical guidelines still apply. In no event shall the Royal Society of Chemistry be held responsible for any errors or omissions in this *Accepted Manuscript* or any consequences arising from the use of any information it contains.

ROYAL SOCIETY
OF CHEMISTRY

www.rsc.org/advances

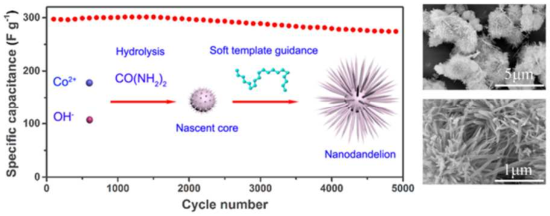

RSC Advances Accepted Manuscript

Journal Name RSCPublishing

ARTICLE

Cite this: DOI: 10.1039/x0xx00000x

Received 00th January 2012,
Accepted 00th January 2012

DOI: 10.1039/x0xx00000x

www.rsc.org/

Dandelion-like Cobalt Hydroxide Nanostructures: Morphological Evolution, Soft Template Effect and Supercapacitive Application

Chen Li, Xiong Zhang, Kai Wang, Haitao Zhang, Xianzhong Sun, Yanwei Ma*

A facile one-pot water bath method has been proposed to synthesize cobalt hydroxide ($Co(OH)_2$) nanodandelions with polyvinyl pyrrolidone (PVP) as soft template. Morphological evolution has been investigated to reveal the crystal growth process of $Co(OH)_2$ and understand the relationship between microstructure and capacitive properties by changing the reaction time and amounts of soft template. The results demonstrate that by rational design of morphology, electrochemical performance of $Co(OH)_2$ can be dramatically enhanced. The unique dandelion-like structure can facilitate both ion and electron diffusion and improve the reaction kinetics, thus offering suitable characteristics for electrode material of high performance supercapacitors. A high specific capacitance of 407 F g^{-1} is obtained, and after 5000 charge-discharge cycles at 10 A g^{-1}, the capacitance retention is still as high as 92%. This work provides an effective method to synthesize hierarchical nanomaterials with high electrochemical capability.

RSC Advances Accepted Manuscript

1. Introduction

Nanomaterials with well-defined shapes and hierarchical morphologies have attracted increasing academic attention because when the size of materials falls into nanoscale, both their physical and chemical properties are dramatically changed [1]. The capability of active materials for electrochemical purposes is significantly influenced by its dimension and morphology since the size reduction of materials increases the electro-active sites accessible to electrolyte, reduces the transport path length for electrons and ions, and promotes the rapid transfer of electrolyte ions across the electrode interface [2]. Therefore, nanostructured electrode materials are expected to provide better electrochemical performance than conventional materials.

Transitional metal oxides/hydroxides, such as Co_3O_4[3], RuO_2[4], Fe_3O_4[5], MnO_2[6], $Ni(OH)_2$[7] and $Co(OH)_2$[8], are generally used as electrode materials for novel energy storage applications. Among them, cobalt hydroxide emerges as a promising candidate for high-performance supercapacitors due to its high specific capacitance (theoretical capacitance up to 3650 F g^{-1}), well-defined electrochemical redox activity, easy synthesis, long cycle life, environmental friendliness and low cost. During the past decades, much effort has been devoted to the design and fabrication of advanced $Co(OH)_2$ nanostructures, including chemical bath deposition [9], hydrothermal route [10], electrochemical deposition[11], solvothermal pathway [12], pulsed laser deposition [13], ball milling [14], γ-Ray induction [15], sonochemical preparation [16] and microwave-assisted synthesis [17]. Based on these methodologies, nanoscale $Co(OH)_2$ with distinct morphologies were obtained, such as nanoparticles[18], nanorods [19], nanowires[20], nanotubes[21], nanocolumns [22], nanowall arrays [23], nanobelts [24], nanodiscs [18], nanoflakes [25], hallow nanohexagons [26], and nanocones [27]. Beside these successes in preparing 1D and 2D $Co(OH)_2$, there are a few reports about the fabrication of novel 3D hierarchical $Co(OH)_2$ nanostructures, represented by rose-like[28], sisal-like[29], carnation-like [30], broom-like [10], butterfly-like [31] morphologies, etc.

It has been widely accepted that only surface atoms or a very thin layer of active electrode materials play a key role during electrochemical processes. From this point of view, electrochemical activities and microstructures of electrode materials are closely linked [32, 33]. Nanoscale materials usually lead to better electrochemical performance than traditional bulk materials because the ion transport distance within the nanostructured electrode materials is dramatically shorter, and the space or holes in the active materials are also beneficial to electrochemical activity. In addition, high charge-discharge rate capability can also be achieved due to the reduction of ion diffusion path. Thus, it is crucial to develop applicable methods to fabricate novel nanoscale materials for electrode purposes. Soft template method is generally considered as an effective way to produce sophisticated nanostructures, due to the self-assembly of nuclei driven by the hydrophilic/hydrophobic interactions and ion pairing between soft template molecules and nuclei. Moreover, the preferential adsorption of soft template on various crystal planes could significantly change

---

Institute of Electrical Engineering, Chinese Academy of Sciences, Beijing, 100190, People's Republic of China
**Corresponding Author. Tel.: +86 10 82547129; Fax: +86 10 82547137; E-mail: ywma@mail.iee.ac.cn*

the growth rate along certain directions, offering a prospect for morphological control of nanoscale materials [34, 35]. Up till now, some progresses have been made through soft templates to selectively control the dimensions of $Co(OH)_2$ for supercapacitor applications. Dodecyl sulfate (DS) was used by Wang et al. to fabricate DS-intercalated $Co(OH)_2$ nanocones with an impressive electrochemical performance of 1055 F g^{-1} at 1 A g^{-1}, but the rate capability was relatively poor, offering only 300 F g^{-1} at 15 A g^{-1} [36]. Zhao et al. adopted N-methylpyrrolidone (NMP) assisted electrochemical deposition route to synthesize α-$Co(OH)_2$ layered structure, which showed a capacitance of 651 F g^{-1} at 2A g^{-1}, and after 500 charge/discharge cycles, 76% of the initial capacitance remained [37]. Ghosh et al. reported a cetyl trimethylammonium bromide (CTAB) assisted hydrothermal pathway to prepare hexagonal nanoplatelet β-$Co(OH)_2$, exhibiting a specific capacitance of 285 F g^{-1} at 2 A g^{-1}, and when graphene was use as the matrix to form composites, the capacitance increased to 532F g^{-1} [38]. Polyethylene glycol (PEG) was used as the structure-directing reagent to produce α-cobalt hydroxides with different intercalated anions [39]. Though the prepared $Co(OH)_2$ showed a high specific capacitance of 697 F g^{-1} at 1 A g^{-1}, there was a 27% capacitance loss after only 100 cycles. A CTAB assisted hydrothermal synthesis was reported by Tang et al. to tune the morphology and grain size of cobalt hydroxide nanocubes and nanowires. The capacitance was 358 F g^{-1} at 2A g^{-1}, and a capacitance retention of 86% after 5000 cycles at 2 A g^{-1} was achieved [40]. Despite all these achievements, the rate capability and cycle performances are not satisfying, and there still lacks a deep-understanding into the relationship between soft template, morphologies and electrochemical performances.

Recently, with hydrazine as coordinating agent, our group reported a facile soft-template assisted water-bath method to prepare $Co(OH)_2$ nanoflowers and nanoplatelets [41]. To further investigate the role of soft template in the fabrication of nanoscale hierarchical materials, we designed a mild urea hydrolysis route to prepare nanoscale dandelion-like $Co(OH)_2$ in the presence of PVP as soft template. The structural and morphological evolution was extensively discussed, and the relationship between morphologies and electrochemical performance was revealed. The dandelion-like $Co(OH)_2$ showed a high specific capacitance of 407 F g^{-1}, a good rate capability, and an excellent capacitance retention of 92% after 5000 charge/discharge cycles at 10 A g^{-1}, which revealed the usefulness of soft template in regulating morphologies and building hierarchical structures to enhance the electrochemical properties of nanomaterials.

2. Experimental

2.1 Preparation of $Co(OH)_2$ nanodandelions

All the chemicals in the experiment were of analytical grade and used without any further treatment. $Co(OH)_2$ nano-dandelions were fabricated by a facile one-pot chemical bath precipitation. For a typical synthesis of $Co(OH)_2$, 1.164 g (4 mmol) $Co(NO_3)_2{\bullet}6H_2O$, 30 g urea ($CO(NH_2)_2$) and 5 g polyvinyl pyrrolidone (PVP, K-30) were dissolved in 50 ml de-ionized water under vigorous stirring at room temperature for 1 h to give a homogeneous transparent solution. Then the resultant mixture was maintained at 80 °C for 6 h in water bath. The purple precipitate was collected by vacuum filtration, washed with deionized water and absolute ethanol for several times to remove the impurities, and dried at 60 °C for 10 h in air. The morphological evolution of $Co(OH)_2$ nanodandelions was studied by changing the reaction time to 2, 4, 8 and 10 h, respectively, while the reaction time was kept at 6 h for all the four samples. To further understand the role of soft template in the assembly of $Co(OH)_2$ nanostructures, 0.5 ,1, 2.5, 10 g PVP were used respectively to prepare samples with different morphologies. For comparison, $Co(OH)_2$ was also synthesized in the absence of PVP.

2.2 Structural and morphological characterization

X-ray diffraction patterns were recorded on a multifunctional X-ray diffractometer (D8, Bruker, German) with monochromatic Cu Kα radiation (λ = 1.54060 Å) at a scanning rate of 10 degree/min. X-ray photoelectron spectroscopy was conducted on a PHI Quantear SXM (ULVAC-PH INC) which used Al as anode probe in 6.7×10^{-8} Pa. The morphology of the synthesized material was investigated by field-emission scanning electron microscope (S4800, Hitachi, Japan). Transmission electron microscopy, high resolution transmission electron microscopy (HRTEM) and selected area electron diffraction (SAED) studies were carried out using a transmission electron microscope (JEOL, JEM 2010F, Japan) operating at an accelerating voltage of 200 kV. The samples were dispersed in ethanol with sonication, and then a drop of the dispersion was placed onto a carbon-coated copper grid and dried at room temperature for 30 min to evaporate the solvent. The Brunauer-Emmett-Teller (BET) surface area was estimated from N_2 adsorption-desorption isotherms at 77 K by Micromeritics ASAP 2020 HD Analyzer. Prior to analysis, all the samples were degassed at 100 °C in vacuum for 12 h. Pore-size distributions were calculated by the Barrett-Joyner-Halenda (BJH) method using the desorption branch of the isotherms. The thermogravimetric (TG) and differential thermogravimetric (DTG) analysis were carried out in N_2 on a Netzsch TG 209 F3 Tarsus from 50 to 500 °C with a heating rate of 5 °C min^{-1}.

2.3 Electrochemical measurements

The working electrode was prepared by pressing a slurry of 70 wt% active material, 20 wt% acetylene black and 10 wt% poly(vinylidene fluoride) (PVDF) in N-methyl-2-pyrrolidone onto a nickel grid (1×1 cm). The electrode was dried at 100 °C for 12 h to evaporate the solvent. The mass of active material on a typical working electrode was about 0.5 mg. All the electrochemical measurements were carried out on a beaker-type three-electrode system, which were equipped with the working electrode, a platinum sheet as the counter electrode, and a standard calomel electrode (SCE) as the reference electrode. 1 M aqueous KOH solution was used as electrolyte. Cyclic voltammetry (CV) and galvanostatic charge-discharge (GCD) tests were performed on an electrochemical workstation (Chenhua, CHI-660, China). CV scans were recorded from -0.2 to 0. 5 V (vs. SCE), and GCD cycle tests were carried out in the range of 0 to 0.4 V. Electrochemical impedance spectroscopy (EIS) measurements were performed under open circuit potential in an frequency range from10, 000 to 0.01 Hz with an excitation signal of 5 mV.

3. Results and Discussion

3.1 Morphological and structural analysis

RSC Advances Accepted Manuscript

This journal is © The Royal Society of Chemistry 2012

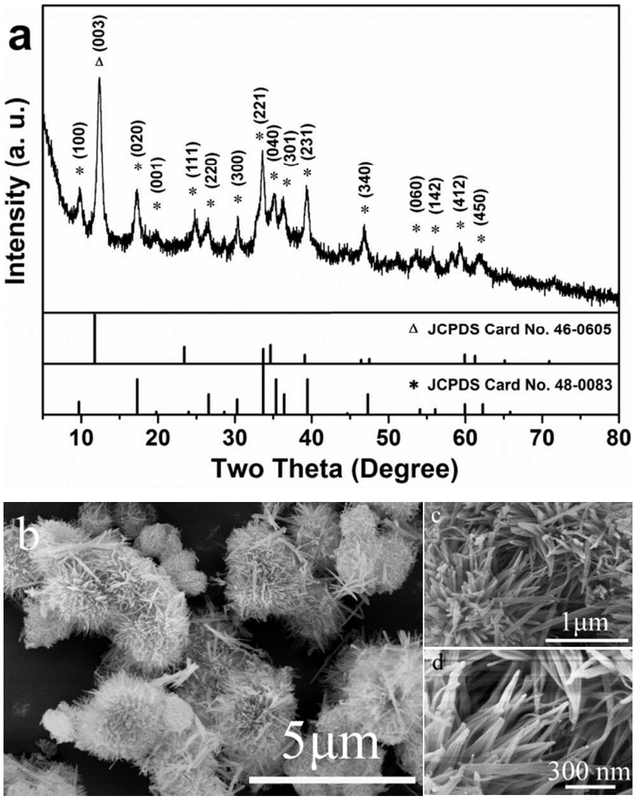

Fig. 1 XRD spectrum (a) and SEM (b-d) images of $Co(OH)_2$ nano-dandelions.

The crystal information of the as-synthesized product is determined by X-ray diffraction (XRD), which is shown in Fig. 1. It can be observed that the sample are composed of α-phase $Co(OH)_2$ intercalated with different ions. The prominent peak at 12.3° can be assigned to (0 0 1) plane of $Co_5(O_{9.48}H_{8.52})NO_3$ (JCPDS card No. 46-0605), while other main peaks correspond perfectly with $Co(CO_3)_{0.5}(OH)\cdot0.11H_2O$ (JCPDS Card No. 48-0083). The results are consistent with previous reports, which successfully synthesize NO_3^- and CO_3^{2-} intercalatedα-phase $Co(OH)_2$ by urea hydrolysis, respectively [42, 43]. SEM and TEM are further used to investigate the microstructure of $Co(OH)_2$ nanodandelions. Fig. 1b-d give a morphological panorama of the $Co(OH)_2$ architectures. It is clearly seen in Fig. 1b that the products show typical dandelion-like structures, with average diameters estimated to be ca. 2.5 μm. The magnified picture in Fig. 1c displays that the 3D hierarchical structures are assembled by well-arranged nanorods extending radially outward. A closer look at Fig. 1d reveals an interesting phenomenon that each nanorod is in fact composed of several sub-rods aligned in parallel, with a twisting at the tip. This suggests that the nanorods are generated from the core simultaneously and at the roughly same growth rate.

TEM image in Fig. 2a shows that a typical sub-rod shows needle-like shape with sharp end of less than 20 nm, broader bottom of about 100 nm, and total axial length around 1 μm. High resolution TEM (Fig. 2b) further gives more information about the crystal structure, in which the (100) and (001) lattice fringes of $Co(CO_3)_{0.5}(OH)\cdot0.11H_2O$ are found to be 8.88 and 4.44 Å, respectively, coinciding perfectly with XRD analysis. The inserted SAED pattern in Fig. 2b exhibits clearly visible diffraction rings, indicating the polycrystalline nature of $Co(OH)_2$ nanodandelions.

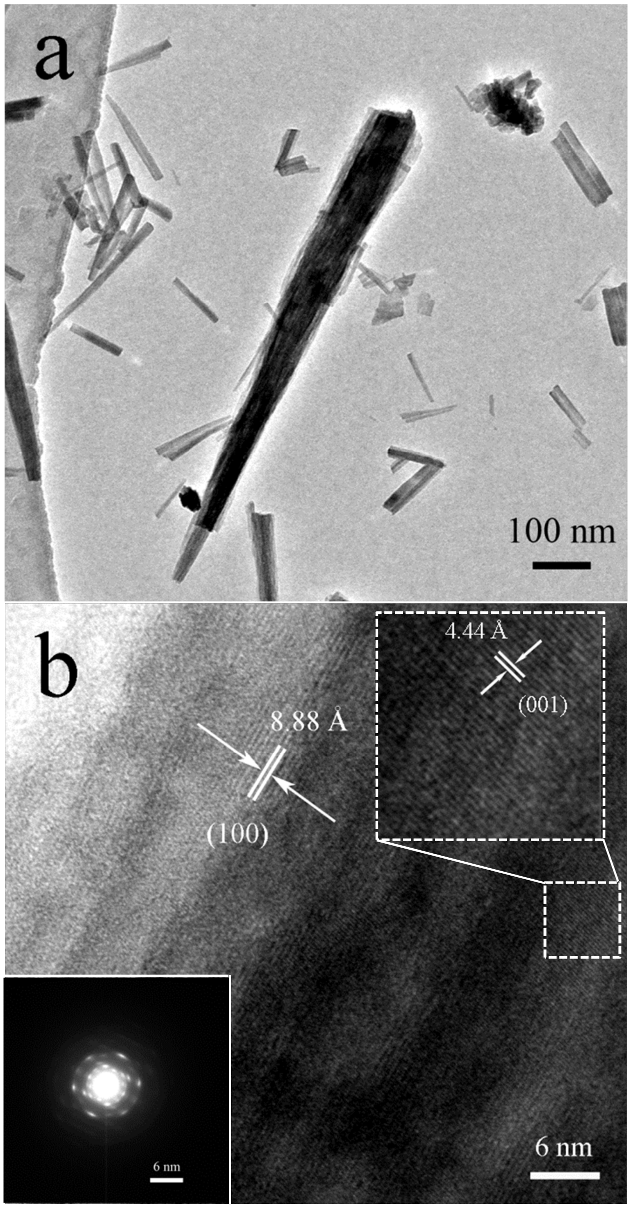

Fig. 2 TEM (a) and HRTEM (b) images of $Co(OH)_2$ nano-dandelions. The inset in (b) gives SAED pattern of the sample.

X-ray photoelectron spectroscopy (XPS) is widely accepted as an effective analytical technique to give surface information by measuring the bonding energy and determine the chemical states of the elements on the surface of the samples. The XPS results of the $Co(OH)_2$ hierarchical nanostructure is shown in Fig. 3. A typical survey of the XPS (Fig. 3a) exhibits four characteristic peaks corresponding to Co 2p, O 1s, N 1s and C 1s. Further investigation into the Co 2p peak (Fig. 3c) shows that the two spin-orbit components of the Co ($2p_{3/2}$) and Co ($2p_{1/2}$) peaks are cantered at 780.4 and 796.0 eV, respectively [19, 23]. A satellite peak on the higher binding-energy side is due to final state effects, which indicates the divalent state of Co ions in the product [44]. The bonding energy has a splitting of 16.1 eV, signifying the presence of Co^{2+} chemical state [20]. The XPS core-level results of O 1s after curve fitting are given in Fig. 3c, in which the broad peak at 532.0 eV is associated with bound hydroxide groups [45], the shoulder peaks at 529.8 eV can be

RSC Advances Accepted Manuscript

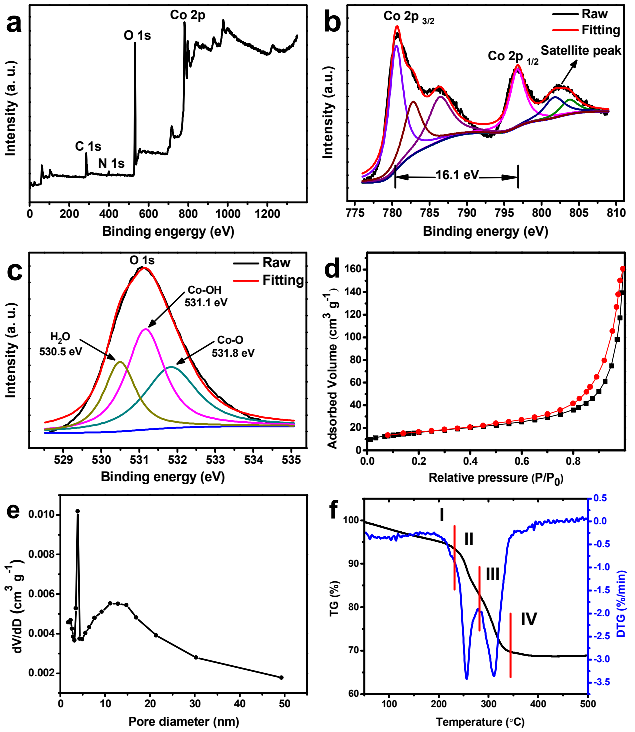

Fig. 3 XPS survey (a), core-level spectra of Co 2p (b) and O 1s (c), N_2 adsorption-desorption isotherm (d), thermogravimetric analysis, pore size distribution curve (e) and differential thermogravimetric analysis (f) of $Co(OH)_2$ nanodandelions.

assigned as Co-O interaction due to a small degree of de-hydroxylation during drying, and the other peak at 532. 8 eV is attributed to structural water in the products [46-48].

The specific surface area and pore size distribution of the sample are calculated by the Brunauer-Emmett-Teller (BET) and Barrett-Joyner-Halenda (BJH) method, respectively. In Fig. 3d, the N_2 adsorption-desorption isotherm of $Co(OH)_2$ nano-dandelions at 77K displays a type IV isotherm according to IUPAC classification and a distinct hysteresis loop (at partial pressure $P/P_0 > 0.4$) due to the featured capillary condensation in the pores, indicating the purely mesoporous nature [49]. The BJH pore size distribution curve derived from the desorption branch (Fig. 3e) reveals the presence of bimodal mesoporosity, in which a narrow pore distribution at ca. 4 nm and a broad pore distribution at around 10-18 nm can be observed. Since the size of the hydrated ions in aqueous electrolyte is typically ranged from 6 to 7.6 Å, $Co(OH)_2$ with pore size in the range of 8-50 Å is considered effective to increase either the pseudo-capacitance or electric double-layer capacitance [50]. The surface area and total pore volume of the product are estimated to be 58 $m^2\ g^{-1}$ and 0.25 $cm^3\ g^{-1}$, respectively.

Thermogravimetric (TG) analysis and differential thermogravimetric (DTG) analysis of $Co(OH)_2$ are performed within the temperature range of 50-500 °C in nitrogen atmosphere, and the curves are represented in Fig. 3e. The weight loss can be easily recognized as a successive four-step process. The first linear weight loss of about 5% in the region of 50-220 °C is associated with the evaporation of physically absorbed water, while the second stage of weight loss of 12% from 220 to 280 °C can be related to the loss of the intercalated water molecules [51]. The third domain ranging from 280 to 345 °C gives a weight loss percentage of 17%, which arises from the loss of water produced by de-hydroxylation of the hydroxide layers combined with the decomposition of the anionic species (CO_3^{2-} and NO_3^-) in α-$Co(OH)_2$ [52]. In region IV, no further weight loss is observed after 345 °C due to the conversion of sample to its corresponding metal oxide Co_3O_4. The total weight loss is 33%, much higher than the theoretical value for stoichiometric β-$Co(OH)_2$ (13.6%), suggesting a different thermogravimetric behaviour of α-$Co(OH)_2$. A similar TG feature of α-$Co(OH)_2$ is also reported by Hu et al[39].

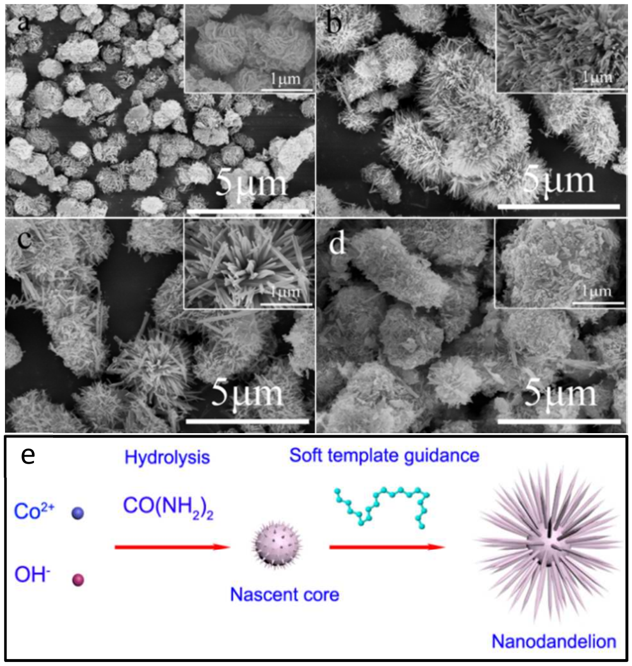

Fig. 4 $Co(OH)_2$ nanostructures synthesized at 2 (a), 4 (b), 8 (c) and 10 h (d). The insets are corresponding magnified images. A schematic illustration of $Co(OH)_2$ nanodandelion growth is given in (e).

3.2 Morphological evolution

Reaction time is generally considered an important parameter in the design and control of hierarchical nanomaterials; therefore, $Co(OH)_2$ are prepared at different time to reveal the morphological evolution and crystal growth mechanism. Fig. 4 shows the time-dependent morphological change of $Co(OH)_2$ nanostructures. It is clearly seen in Fig. 4a that at a short reaction time of 2 h, the samples are mostly composed of spherical particles with uniform diameters around 1 μm. The inset shows that the crumpled surface is caused by the outward growth of randomly interconnected nanoflakes. However, when the time is prolonged to 4 h, a sharp difference in morphology appears (Fig. 4b). The nascent nano-dandelion structure has average size of 2 μm, suggesting that the nanostructure is developed form a core. Compared with the size (2.5 μm) of samples prepared at 6 h (see Fig. 1b), it can be inferred that the nanorods are relatively shorter in length. A careful examination of the inset reveals that the nanorods are arranged in a relatively compact manner, probably because that the shorter length of nanorod cannot afford the flexibility to present a loose morphology. Further increasing the time to 8h (Fig. 4c), though the dandelion-like structure can still be recognized, the nanorods are becoming thicker to leave larger space in between. Extending the time for another two hours, no traces of

RSC Advances Accepted Manuscript

This journal is © The Royal Society of Chemistry 2012

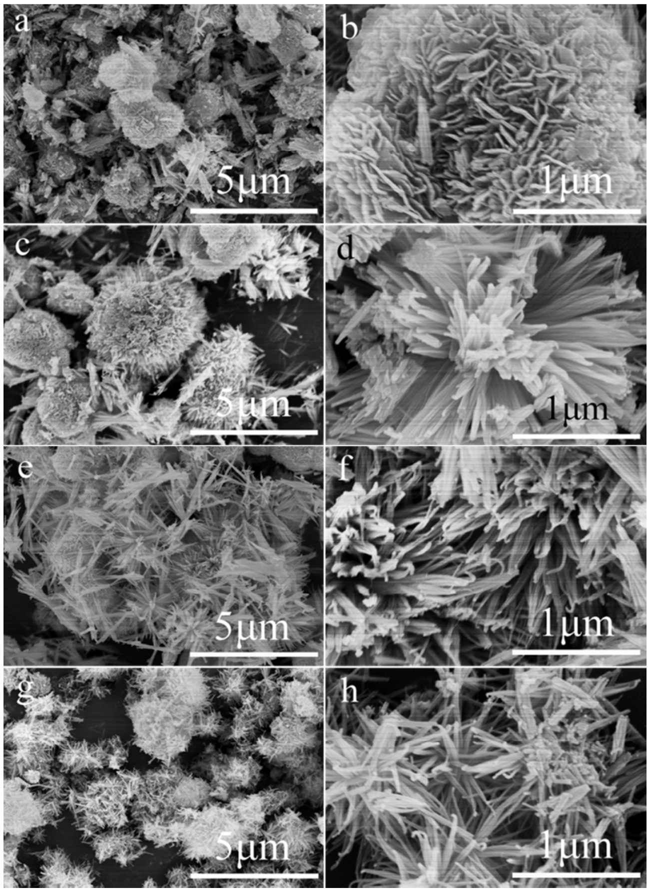

Fig. 5 $Co(OH)_2$ nanostructures synthesized without PVP (a-b), and with 0.5 (c-d), 2.5 (e-f), and 10 g (g-h) PVP.

dandelion-like structure can be recognized (Fig. 4d). The products are aggregated into irregular particles with sizes about 2-4 μm, due to the partial overlapping and merging of previous nanodandelions. The dense surfaces shown in the inset implies that the continual lateral growth of nanorods fill the space in the nanostructure and combine closely to give a compact and ill-defined morphology.

Based on the investigation into morphological evolution, the possible growth mechanism of $Co(OH)_2$ nanodandelions can be reasonably summarized as a three-step process: (1) formation of nascent nanoparticles as the core, (2) growth of nanorods on the core to give dandelion-like shape, (3) continual development of nano-dandelions into larger nanoparticles. In the first step, the hydrolysis of urea produces an alkaline condition to precipitate the Co^{2+} ions in the system according to the reactions:

$$CO(NH_2)_2 + H_2O \rightarrow 2\ NH_3 + CO_2 \quad (1)$$

$$CO_2 + H_2O \rightarrow 2\ H^+ + CO_3^{2-} \quad (2)$$

$$NH_3 + H_2O \rightarrow NH_4^+ + OH^- \quad (3)$$

The newly formed $Co(OH)_2$ nuclei quickly aggregate into uniform spherical particles, offering the core for following growth. The soft template plays an important role in the second stage, which guides the outward growth of nanorods on the core to prepare dandelion-like hierarchical structures. The whole process occurs with a view to minimize the surface energy [53]. Due to the slow hydrolysis of urea, OH^- ions are offered at a quasi-constant rate to control the kinetics of $Co(OH)_2$ formation, which provides enough space and time for the simultaneous development of nanorods. As the reaction time is prolonged, the nanorods gradually grow both axially and laterally to fill the space in the dandelions; therefore, the third period produces more compact and larger nanoparticles. A schematic illustration of the crystal growth process is given in Fig. 4e.

It is well-known that the selective guidance of soft template on various crystallographic planes of the precursors during the crystal growth could produce distinct morphologies [54]. To further understand the relationship between soft template and nanostructure, different amounts of PVP are used to give various $Co(OH)_2$ nanostructures. Without PVP in the system (Fig. 5a), only irregular nanoparticles with coral-like surface are obtained, which bear much morphological resemblance to Fig. 1a, except for their much larger sizes (ca. 3 μm). This implies that without soft template to guide crystal growth, no ordered hierarchical structures can be obtained. When 0.5 g PVP is used, crude dandelion-like structure with average diameter of 2.5 μm appears (Fig. 5c), and the magnified image in Fig. 5d shows the compact alignment of nanorods in the structure. Further raising the amount of PVP to 2.5 g, it can be clearly recognized that nanodandelions are formed (Fig. 5e). Some individual nanorods are present in the picture, which might be due to the insufficient cohesion with the core. Fig. 5f shows that the several nanorods on the dandelions are grown along the axis into a strand, with a twisting at the tips. As the PVP iss increased to 10 g, a loosely packed dandelion-like structure develops, presenting a smaller average size of 1 μm. The nanorods on each dandelion are around 600 nm in length with hook-like ends, and are obviously less in number compared with the products with 5 g PVP (see Fig. 1b), which suggests that too much soft template would destroy 3D hierarchical structures. The analysis above clearly indicates that soft template plays a crucial role in the control of $Co(OH)_2$ morphologies.

The phase evolution during the synthesis of the products has been measured by powder X-ray diffraction. Fig. 6a gives the XRD patterns of $Co(OH)_2$ nanostructures obtained at different reaction time. It is well-known that the hydrotalcite-like α-hydroxide consists of stacked positively charged $Co(OH)_{2-x}$ layers intercalated with various balancing anions (e.g. NO_3^-, CO_3^{2-}, Cl^-, SO_4^{2-}, CH_3COO^-, etc.) in the interlayer gallery to restore charge neutrality [36]. These anions are highly exchangeable with each other, which may offer a possible path for phase transformation [55]. It can be observed in Fig. 6a that when the reaction time is 2 h, all the diffraction peak can be assigned to the hexagonal phase of $Co_5(O_{9.48}H_{8.52})NO_3$ [17]. As the reaction prolongs to 4 h, (0 0 3), (0 0 6) and (1 1 0) peaks of NO_3^- intercalated α-$Co(OH)_2$ weakens, and diffraction peak belonging to orthorhombic $Co(CO_3)_{0.5}(OH)\bullet 0.11H_2O$ gradually appears [43], suggesting that NO_3^- ions in the interlayer galleries are gradually substituted by CO_3^{2-}. This phenomenon becomes more obvious at 10 h, in which the (0 0 3) peak corresponding to $Co_5(O_{9.48}H_{8.52})NO_3$ fades sharply while the diffraction peaks of $Co(CO_3)_{0.5}(OH)\bullet 0.11H_2O$ are dominant. This can be explained by the slow hydrolysis rate of urea. At the initial stage of the reaction, the dissolved $Co(NO_3)_2$ provide abundant NO_3^- ions, while the CO_3^{2-} produced from urea are relatively deficient; therefore, NO_3^- intercalated $Co(OH)_2$ is mainly

RSC Advances Accepted Manuscript

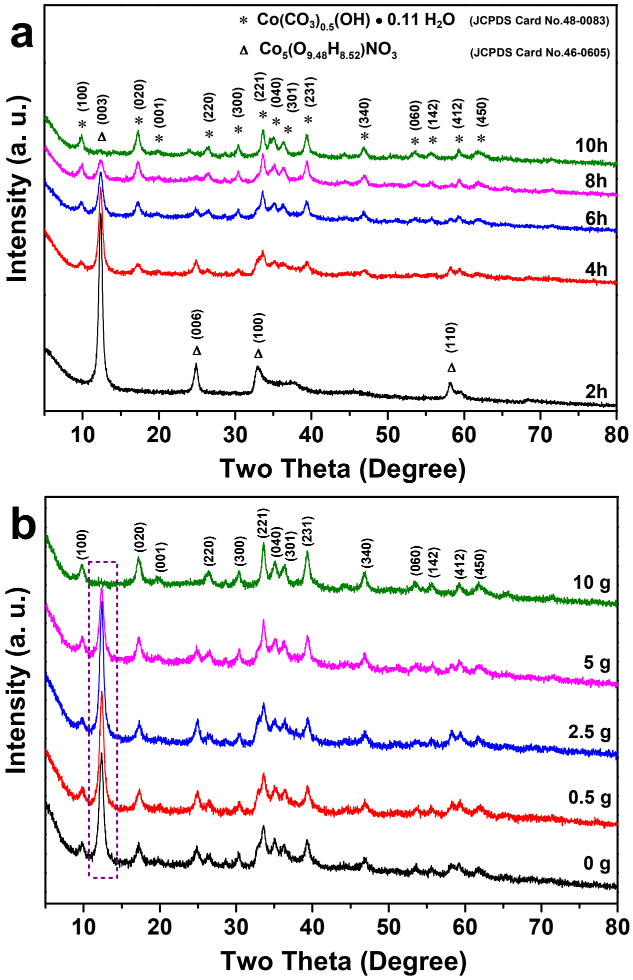

Fig. 6 XRD of $Co(OH)_2$ synthesized for different time (a) and with different amounts of PVP (b).

formed. However, a longer reaction time causes a higher hydrolysis degree of urea, which offers sufficient CO_3^{2-} to make ion exchange possible [56]. The OH^- and CO_3^{2-} ions provided by the slow hydrolysis of urea together with the guidance of soft template would probably favour the gradual growth of the nanorods along their longitudinal axis [43].

To investigate the effect of soft template on the phase transformation of products, XRD measurements of $Co(OH)_2$ obtained with different amounts of PVP are given in Fig. 6b. As illustrated in the dash-lined area, without soft template, a prominent (0 0 3) peak can be clearly recognized, representing the NO_3^- intercalated α-$Co(OH)_2$ existed in the samples. Further increasing the amount of PVP in the reaction system, the intensity of (0 0 3) peak reduces and finally disappears when 10 g PVP is used, while the peaks corresponding to α-$Co(OH)_2$ intercalated with CO_3^{2-} are gradually enhanced, suggesting the orthorhombic phase are more apt to form in high PVP concentration systems. The results confirms that soft template has an important effect on the composition of $Co(OH)_2$ nanostructures.

3.3 Electrochemical measurement

3.3.1 Cyclic voltammetry

The electrochemical properties the $Co(OH)_2$ nanostructures are characterized by cyclic voltammetry in 1 M KOH aqueous solution at the voltage window of -0.2-0.5 V, and the results are shown in Fig. 7. This potential range is determined by the intrinsic properties of cobalt hydroxide, which causes oxygen evolution when the voltage is higher than 0.5 V and exhibits no redox activity below -0.2 V [37]. Fig. 7a gives the CV curves of $Co(OH)_2$ nanodandelions at different scan rates, in which two pairs of redox peaks can be easily observed in the voltage range of 0-0.1 V and 0.25-0.35 V. The surface redox processes can be related to the following two electrochemical reactions [57]:

(i) anodic P1 and cathodic P2 correspond to the transformation:

$$Co(OH)_2 + OH^- \rightarrow CoOOH + H_2O + e^- \tag{4}$$

(ii) anodic P3 and cathodic P4 should be ascribed to the conversion:

$$CoOOH + OH^- \rightarrow CoO_2 + H_2O + e^- \tag{5}$$

The distinct redox peaks and the non-rectangular shape of CV curves indicate that the electrochemical properties of $Co(OH)_2$ nanodandelions mainly comes from faradic pseudocapacitance, which utilizes the fast electron-transfer at electrode surface. The characteristic symmetry of the anodic and cathodic peaks and high redox current suggest the excellent electrochemical reversibility for $Co(OH)_2$ as active materials for electrode [58]. As the scan rate increases from 5 to 100 mV s^{-1}, CV curves change little in shape, suggesting good electron conduction within the nanodandelion over a wide range of potential scan rates. The anodic P1 and P3 shift positively while cathodic P2 and P4 move to the negative voltage side due to the internal resistance of the electrode [59]. To further study the kinetics of redox processes, the fitting analysis of anodic peak current (i_p) vs. scan rate (V), and anodic peak current (i_p) vs. the square root of scan rate ($V^{1/2}$) is performed. In an absorption process, it is

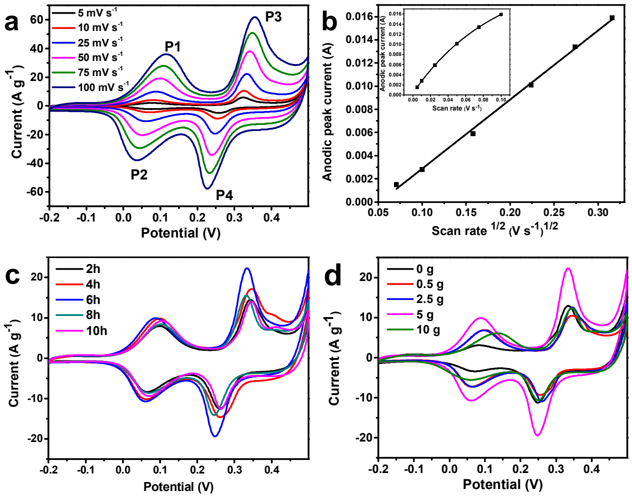

Fig. 7 Cyclic voltammetry curves of $Co(OH)_2$ nanodandelions at different san rates (a); i_p vs. $V^{1/2}$ (b) and i_p vs. V (inset in b) plots of $Co(OH)_2$ nanodandelions; cyclic voltammetry curves of $Co(OH)_2$ synthesized under various reaction time (c) and with different amounts of PVP (d) at scan rate of 25 mV s^{-1}.

RSC Advances Accepted Manuscript

This journal is © The Royal Society of Chemistry 2012

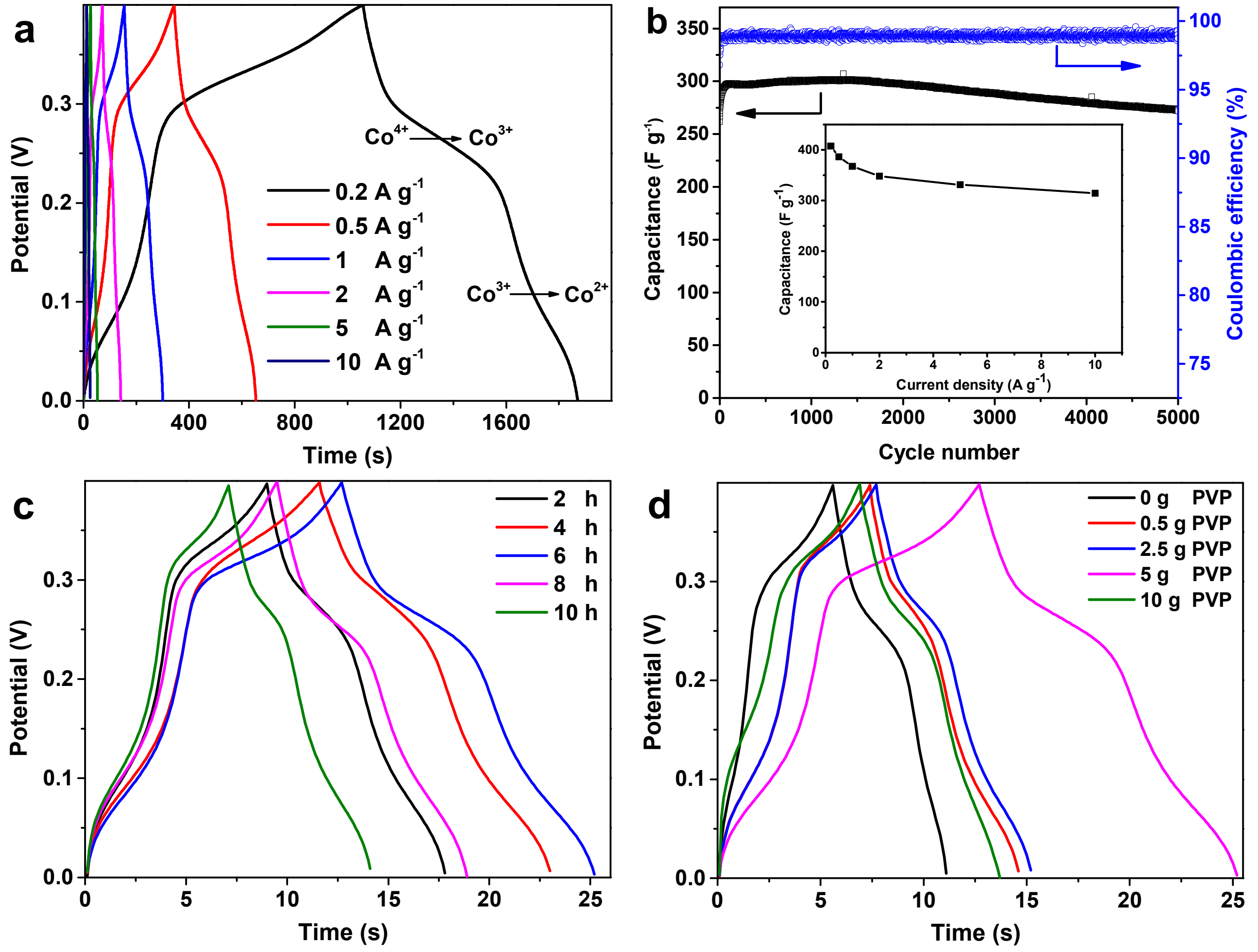

Fig. 8 Galvanostatic charge-discharge curves of $Co(OH)_2$ nanodandelions at different current densities (a); cycle life performance at 10 A g^{-1} (b), rate capability of $Co(OH)_2$ nanodandelions (inset in b); charge-discharge curves of $Co(OH)_2$ synthesized under different reaction time (c) and with different amounts of PVP (d) at 10 A g^{-1}.

Table 1. Comparative cyclic performance of $Co(OH)_2$ nanostructures prepared by chemical methods.

Morphology	Current density (A g^{-1})	Cycle number (n)	Capacitance retention (%)	Ref.
Nanocone	2	3000	88	[27]
Nanorod	10	1000	74	[19]
Nanowire	2	5000	86	[40]
Nanoflower	1	500	93	[60]
Hexagonal nanoplate	0.5	1000	90	[16]
Nanosheet	0.5	500	78	[61]
Nanowire	0.4	1000	75	[62]
Nanodandelion	10	5000	92	This work

proposed that within a reasonable range of scan rates, i_p vs. V should exhibit a linear relationship [15]. On the other hand, for semi-infinite diffusion-limited reaction in aqueous electrolytes, the relationship of i_p vs. $V^{1/2}$ is expected to be linear for different scan rates [37, 39]. It can be clearly seen from Fig. 7b that the plot of anodic peak current i_p vs. $V^{1/2}$ gives a perfect linear relationship, while the curve of i_p vs. V is obviously nonlinear. Based on this analysis, it is safe to conclude that the redox reaction of $Co(OH)_2$ nanodandelions corresponds to diffusion-controlled process. Fig. 7c gives the CV curves of $Co(OH)_2$ nanostructures synthesized at different reaction time at 25 mV s^{-1} scan rates within a potential window from -0.2 to 0.5 V. It is noted that all the samples are similar in

RSC Advances Accepted Manuscript

shape with two pairs of prominent redox peaks corresponding to the pseudocapacitive properties. However, the sample prepared at 6 h shows the largest area compared with other four products, which indicates its excellent capacitance. It is suggested that the space between adjacent $Co(OH)_2$ nanorods serves as "buffering reservoirs" for electrolyte ions during electrochemical processes, which ensures that sufficient Faradaic reaction can take place [36]. CV curves of $Co(OH)_2$ produced with different amounts of soft template are shown in Fig. 7d. An analogous situation can be observed that dandelion-like architecture obtained with 5 g PVP exhibits the optimal capacitive performance.

3.3.2 Galvanostatic charge-discharge tests

Galvanostatic charge-discharge measurement is employed to further study the electrochemical properties of $Co(OH)_2$ nanostructures. The test is carried out within the limited voltage range of 0-0.4 V because higher potential would result in a very low columbic efficiency [38]. Fig. 8a shows the GCD curves of the as-prepared $Co(OH)_2$ nanodandelions at various charge-discharge current densities. All the plots show symmetric semi-triangular shape with well-defined plateaus, which are consistent with the results of the CV analysis. The obvious deviation of the curves from linearity suggests the capacitance comes mainly from pseudocapacitance involved in the fast reversible surface redox reaction, instead of double layer capacitance which is related with purely physical separation of charges at the electrode interface. The switching at around 0.25V arises from the oxidation of $Co(OH)_2$ to CoOOH (P1 and P2), and the turning at about 0.1 V should be ascribed to the conversion of CoOOH to CoO_2 (P3 and P4). The specific capacitance is a function of current density, which can be expressed as the following equation [63]:

$$C_s = \frac{I\,\Delta t}{m\,\Delta V} \tag{6}$$

in which C_s (F g^{-1}) is the specific capacitance, I (A) denotes the discharge current, Δt (s) refers to the discharging time, ΔV (V) stands for the potential window, and m (g) represents the mass of active material on the electrode. The specific capacitances of $Co(OH)_2$ nanodandelion at 0.2, 0.5, 1, 2, 5 and 10 A g^{-1} are calculated to be 407, 386, 367, 348, 331 and 314 F g^{-1}, respectively. The high specific capacitance at 0.2 A g^{-1} is featured by the slight ohmic drop and open access provided by inner active sites in the electrode to electrolyte ions, while the lower capacitance at larger current densities is mainly caused by the increase in ionic resistivity and insufficient utilization of electrode surface. The areal specific capacitance can be obtained from the formula:

$$C_A = \frac{C_s}{S} \tag{7}$$

where S corresponds to the specific surface area given by BET method. The dandelion-like structure has an areal specific capacitance of 7.01 F m^{-2}, which is higher than $Co(OH)_2$ nanocones (5.4 F m^{-2}) [27], nanoflowers (2.19 F m^{-2}) [60], and coral-like nanostructures (1.52 F m^{-2}) [45], demonstrating again the advantages of dandelion-like structure for high capacitive performance in redox processes.

Stability test of electrode material is carried out at a high current density of 10 A g^{-1} in 1 M KOH for 5000 continuous cycles (Fig. 8b). The active material experienced an obvious electrochemical activation in the first 200 cycles, and remained nearly unchanged for the next 1000 cycles. Then the capacitance began to slightly decrease, and after the cycle life test, the electrode material gives an impressive capacitance retention percentage of 92%, which is superior to the recently reported values based on chemical method (see Table1).The slight capacitance loss of 8% is probably due to the following reasons: (1) the inevitable chemical decay resulted from the swelling and shrinkage of electrode material by ion intercalation makes it difficult to maintain the structure integrity as well as the intact initial morphology[23]; (2) the physical connection by binder adhesion to current collector is not robust, and some active material may drop from the electrode during consecutive charge-discharge process owing to the stress damage, and naturally result in slight capacitance loss; (3) the metastable α-$Co(OH)_2$ in alkaline KOH electrolyte probably experiences a phase transformation to β-$Co(OH)_2$, which generally has a lower capacitance due to its narrower interplanar spacing[64]. Moreover, the rate capability of $Co(OH)_2$ nanodandelions (inset in b) are also tested. The capacitances at low current densities (0.2 and 0.5 A g^{-1}) are very close in quantity, suggesting the almost complete charge-discharge behaviour in redox process [26]. Besides, the capacitance still remains 77% when the current density increases from 0.2 to 10 A g^{-1}, which demonstrates the stability of pseudocapacitive behaviour at high current rates. The coulombic efficiency (η) can be calculated by Eq. (8):

$$\eta = \frac{t_D}{t_C} \times 100\% \tag{8}$$

in which t_D and t_C stand for charge and discharge time, respectively. The coulombic efficiency of the electrode remains higher than 98% all through the cycle life test except the initial several activation cycles, indicating its high redox reversibility, low internal resistance and excellent energy utilization rate. The results implies that hierarchical $Co(OH)_2$ nanostructures have a prospect for supercapacitors with long-term cycle stability.

The high electrochemical properties of dandelion-like structures could be ascribed to the following three reasons: (i) The nanopores and mesopores in $Co(OH)_2$ nanodandelions can offer open channels for the fast diffusion of electrons within the redox phase. (ii) The space in the nanostructures can act as an 'ion buffering reservoir' to provide steady supply of OH^- ions during the pseudocapacitive process, shorten the ion transportation length, and facilitate maximized contact with electrolyte and rapid transfer of ions, which enhance the kinetics of reversible interfacial reaction for charge storage. (iii) The abundant space in the 3D hierarchical structure can effectively accommodate the swelling and shrinkage of electrode materials during charge-discharge process to avoid electrochemical decay.

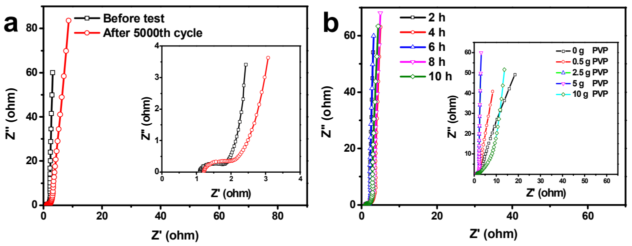

Fig.8 Nyquist plots of $Co(OH)_2$ nanodandelions before (a) and after GCD cycling test; EIS of $Co(OH)_2$ synthesized at different time (b) and with different amounts of PVP (inset).

RSC Advances Accepted Manuscript

This journal is © The Royal Society of Chemistry 2012

The capacitive behaviour of $Co(OH)_2$ nanostructures is further investigated to better understand the relationship between morphologies and electrochemical properties. Fig. 8c gives the charge-discharge performance of $Co(OH)_2$ prepared at different time. The specific capacitance at 10 A g^{-1} for $Co(OH)_2$ synthesized at 2, 4, 6, 8 and 10 h are calculated to be 221, 283, 314, 235 and 152 F g^{-1}, respectively. At a shorter time of 2 and 4 h, the particles and immature dandelions could not provide enough transportation channels for rapid mass transfer, which results in a relatively low capacitance. When the time is extended to 6 h, the active sites in the fully developed 3D hierarchical structure can be efficiently utilized, thus giving the optimum electrochemical performance. However, further increasing the reaction would cause the random aggregation of hierarchical structures and final formation of bulky particles, which are detrimental for the contact with electrolyte. As a result, poor capacitive behaviour is observed. The effect of soft template on the electrochemical performance is presented in Fig. 8d. The results are consistent with the CV analysis. The specific capacitances are 138, 170, 188, 313, 175 F g^{-1} for $Co(OH)_2$ obtained with 0, 0.5, 2.5, 5, 10 g PVP, respectively, which can also be explained by morphological features. Without PVP as guiding agent for crystal growth, the randomly aggregated $Co(OH)_2$ nanostructures only offer limited active sites for redox reaction. As the amount of soft template in the system increases, the $Co(OH)_2$ gradually become hierarchical, and more electrode materials can participate in the electrochemical process to enhance the capacitive performance. However, excessive soft template produces an ill-defined morphology, hampering the efficient utilization of electrode materials.

3.3.3 Electrochemical impedance spectroscopy

It has been commonly acknowledged that EIS analysis is an effective method to reveal the capacitive behaviour of electrode materials for supercapacitors [65]. To further understand the redox process, Nyquist plots of $Co(OH)_2$ nanodandelions before cycling test and after 5000 cycles are given in Fig. 9a. It should be noted that both spectra are highly similar in form, with a vertical spike at a low frequency domain and an arc at a high frequency region, indicating the impressive electrochemical stability of dandelion-like nanomaterials. The intersection of the high frequency region at the real axis corresponds to the equivalent series resistance (ESR) of electrode, which generally includes three parts: the resistance of electrolyte, the intrinsic resistance of electroactive material and the contact resistance at the interface between electrode materials and current collector. The value of ESR determines the rate the electrode can be charged/discharged (power capability), crucial to the power density of a supercapacitor [66]. From the inset in Fig. 9a, the ESR before GCD test is found to be a rather small value around 1.07 Ω, because the unique dandelion-like structure not only facilitates the easy diffusion and penetration of electrolyte ions but also effectively shortens the ion diffusion length. After the cycling test, the ESR increases slightly to 1.22 Ω, suggesting that the excellent electrochemical conductivity and rate capability of $Co(OH)_2$ nanodandelions can still remain even after the long-time cycling test at large current density. The charge transfer resistance (R_{ct}) can be calculated from the diameter of semicircle at high frequency region. The $Co(OH)_2$ nanodandelions give small R_{ct} values of 0.53 and 0.71 Ω before and after the test, respectively, which indicates the faster electron-transfer rate during redox process. In the intermediate-frequency region, a short 45° line can be seen, suggesting the existence of finite length Warburg resistance caused by the frequency dependence of ion diffusion/transport from the surface into the porous structure of the electrode[67]. Furthermore, in the low frequency region, both plots exhibit a vertical line representative of the diffusion and migration of the electrolyte ions within the electrode structure, demonstrating good capacitive behaviour of the as-prepared hierarchical nanostructure.

Fig. 9b depicts the EIS of $Co(OH)_2$ synthesized at different reaction time, which share almost the same shape throughout the frequency range. Nevertheless, the $Co(OH)_2$ nanodandelions obtained at 6 h present a more vertical line at low frequency region, which is consistent with CV and GCD analysis, confirming its superior capacitive performance than other products. The inset in Fig. 9b is the Nyquist plots of $Co(OH)_2$ prepared with different amounts of PVP. It can be clearly observed that $Co(OH)_2$ obtained without PVP shows a 70° line at low frequency region, revealing its relatively poor capacitive properties. A small amount of PVP (0.5 g) makes the line lean more toward the imaginary axis at low frequencies. When PVP is increased to 2.5 and 5 g, a perfect vertical line appears, suggesting that proper amount of PVP is beneficial for capacitive properties. However, excessive PVP (10 g) present a longer Warburg resistance range due to difficult ion diffusion and electron transport into the interior of electrode. The EIS analysis clearly illustrates that soft template has an important role in electrode process, which is expected to be controlled through the interaction between the soft template and crystal morphologies.

Conclusion

In this paper, we adopted a facile, cost-saving and controllable chemical bath pathway for the fabrication of $Co(OH)_2$ nanodandelions as electrode material. PVP was used as guiding agent to control the morphologies of $Co(OH)_2$ crystals. XRD and XPS were performed to investigate the crystal structure. BET method showed that the nanodandelions had a typical mesoporous structure with specific surface area of 58 m^2 g^{-1}. The thermal stability of $Co(OH)_2$ crystals was studied by TG analysis. The morphological evolution was extensively discussed to reveal the relationship between morphologies and electrochemical performances. $Co(OH)_2$ nanodandelions exhibited a high specific capacitance of 407 F g^{-1} at 0.2 A g^{-1}, and still remained 314 F g^{-1} at 10 A g^{-1}. Impressively, the electrode material kept 92% of its original capacitance after 5000 cycles at 10 A g^{-1}, demonstrating the excellent electrochemical stability. This work confirms the potentiality of soft template in the design and control of hierarchical electrode materials, which may offer an example for future synthesis of novel nanostructures for supercapacitors.

Acknowledgements

This work was financially supported by the National Natural Science Foundation of China (Nos. 51472238 and 51025726), and the Open Project Program of State Key Laboratory of Chemical Resource Engineering (CRE-2014-C-102).

Reference

1. M. A. El-Sayed, *Acc. Chem. Res.*, 2004, **37**, 326-333.
2. K. Wang, H. Wu, Y. Meng and Z. Wei, *Small*, 2014, **10**, 14-31.

RSC Advances Accepted Manuscript

3. H. Xia, D. Zhu, Z. Luo, Y. Yu, X. Shi, G. Yuan and J. Xie, *Sci Rep*, 2013, **3**, 2978.
4. Y. Chen, X. Zhang, D. C. Zhang and Y. W. Ma, *J. Alloys Compd.*, 2012, **541**, 415-420.
5. Y. Chen, H. Xia, L. Lu and J. Xue, *J. Mater. Chem.*, 2012, **22**, 5006.
6. D. Zhu, Y. Wang, G. Yuan and H. Xia, *Chem. Commun.*, 2014, **50**, 2876-2878.
7. H. B. Li, M. H. Yu, F. X. Wang, P. Liu, Y. Liang, J. Xiao, C. X. Wang, Y. X. Tong and G. W. Yang, *Nat. Commun.*, 2013, **4**, 1894.
8. Y. Wang, H. Xia, L. Lu and J. Y. Lin, *ACS Nano*, 2010, **4**, 1425-1432.
9. W. Z. Z. Wang, Q. Zhou, L. J. Wang, T. Yang and G. L. Zhang, *J. Cryst. Growth*, 2010, **312**, 3485-3489.
10. B. X. Wang, H. Lin and Z. G. Yin, *Mater. Lett.*, 2011, **65**, 41-43.
11. V. Gupta, T. Kusahara, H. Toyama, S. Gupta and N. Miura, *Electrochem. Commun.*, 2007, **9**, 2315-2319.
12. W. E. Mahmoud and T. Al-Harbi, *Mater. Lett.*, 2011, **65**, 1986-1988.
13. Y. L. Wang, H. W. Wang and X. F. Wang, *Electrochim. Acta*, 2013, **92**, 298-303.
14. L. Y. Gong and L. H. Su, *Appl. Surf. Sci.*, 2011, **257**, 10201-10205.
15. J. M. Ko, D. Soundarajan, J. H. Park, S. D. Yang, S. W. Kim, K. M. Kim and K. H. Yu, *Curr. Appl. Phys.*, 2012, **12**, 341-345.
16. X. H. Liu, B. H. Qu, F. H. Zhu, L. Y. Gong, L. H. Su and L. Q. Zhu, *J. Alloys Compd.*, 2013, **560**, 15-19.
17. T. Yan, H. Y. Zhu, R. Y. Li, Z. J. Li, J. K. Liu, G. L. Wang and Z. Q. Gu, *Electrochim. Acta*, 2013, **111**, 71-79.
18. M. Aghazadeh, H. M. Shiri and A. A. M. Barmi, *Appl. Surf. Sci.*, 2013, **273**, 237-242.
19. U. M. Patil, S. C. Lee, J. S. Sohn, S. B. Kulkarni, K. V. Gurav, J. H. Kim, J. H. Kim, S. Lee and S. C. Jun, *Electrochim. Acta*, 2014, **129**, 334-342.
20. T. Xue and J.-M. Lee, *J. Power Sources*, 2014, **245**, 194-202.
21. X. W. Lou, D. Deng, J. Y. Lee, J. Feng and L. A. Archer, *Adv. Mater.*, 2008, **20**, 258-262.
22. Y. Z. Shao, J. Sun and L. Gao, *J. Phys. Chem. C*, 2009, **113**, 6566-6572.
23. A. Ramadoss and S. J. Kim, *Electrochim. Acta*, 2014, **136**, 105-111.
24. C. Z. Yuan, L. Yang, L. R. Hou, D. K. Li, L. F. Shen, F. Zhang and X. G. Zhang, *J. Solid State Electrochem.*, 2012, **16**, 1519-1525.
25. L. B. Kong, J. W. Lang, M. Liu, Y. C. Luo and L. Kang, *J. Power Sources*, 2009, **194**, 1194-1201.
26. D. Zhou, X. Su, M. Boese, R. Wang and H. Zhang, *Nano Energy*, 2014, **5**, 52-59.
27. F. Cao, G. X. Pan, P. S. Tang and H. F. Chen, *J. Power Sources*, 2012, **216**, 395-399.
28. B. X. Li, Y. Xie, C. Z. Wu, Z. Q. Li and J. Zhang, *Mater. Chem. Phys.*, 2006, **99**, 479-486.
29. X. Tan, H. Gao, M. Yang, Y. Luan, W. Dong, Z. Jin, J. Yu, Y. Qi, Y. Feng and G. Wang, *J. Alloys Compd.*, 2014, **608**, 4.
30. L. X. Yang, Y. J. Zhu, L. Li, L. Zhang, H. Tong, W. W. Wang, G. F. Cheng and J. F. Zhu, *Eur. J. Inorg. Chem.*, 2006, **2006**, 4787-4792.
31. J. T. Sampanthar and H. C. Zeng, *J. Am. Chem. Soc.*, 2002, **124**, 6668-6675.
32. Q. Lu, J. G. Chen and J. Q. Xiao, *Angew. Chem. Int. Ed.*, 2013, **52**, 1882-1889.
33. S. Chen, W. Xing, J. Duan, X. Hu and S. Z. Qiao, *J. Mater. Chem. A*, 2013, **1**, 2941.
34. N. Pal and A. Bhaumik, *Adv. Colloid. Interface. Sci.*, 2013, **189-190**, 21-41.
35. N. Sahiner, *Prog. Polym. Sci.*, 2013, **38**, 1329-1356.
36. L. Wang, Z. H. Dong, Z. G. Wang, F. X. Zhang and J. Jin, *Adv. Funct. Mater.*, 2013, **23**, 2758-2764.
37. T. Zhao, H. Jiang and J. Ma, *J. Power Sources*, 2011, **196**, 860-864.
38. D. Ghosh, S. Giri and C. K. Das, *ACS Sustainable Chem. Eng.*, 2013, **1**, 1135-1142.
39. Z. A. Hu, Y. L. Xie, Y. X. Wang, L. J. Xie, G. R. Fu, X. Q. Jin, Z. Y. Zhang, Y. Y. Yang and H. Y. Wu, *J. Phys. Chem. C*, 2009, **113**, 12502-12508.
40. Y. F. Tang, Y. Y. Liu, S. X. Yu, S. C. Mu, S. H. Xiao, Y. F. Zhao and F. M. Gao, *J. Power Sources*, 2014, **256**, 160-169.
41. C. Li, X. Zhang, P. Yu, H. Zhang, X. Sun and Y. Ma, *Crystengcomm*, 2014, **16**, 7478.
42. T. N. Ramesh, *Inorg. Chem. Commun.*, 2011, **14**, 419-422.
43. B. Wang, T. Zhu, H. B. Wu, R. Xu, J. S. Chen and X. W. Lou, *Nanoscale*, 2012, **4**, 2145-2149.
44. T. Xue, X. Wang and J. M. Lee, *J. Power Sources*, 2012, **201**, 382-386.
45. S. C. Tang, S. Vongehr, Y. Wang, L. Chen and X. K. Meng, *J. Solid State Chem.*, 2010, **183**, 2166-2173.
46. J.-C. Dupin, D. Gonbeau, P. Vinatier and A. Levasseur, *Phys. Chem. Chem. Phys.*, 2000, **2**, 1319-1324.
47. C.-H. Lien, J.-C. Chen, C.-C. Hu and D. S.-H. Wong, *J. Taiwan Inst. Chem. Eng.*, 2014, **45**, 846-851.
48. R. Xu and H. C. Zeng, *Chem. Mater.*, 2003, **15**, 2040-2048.
49. X. Zhang, X. Z. Sun, H. T. Zhang, D. C. Zhang and Y. W. Ma, *Electrochim. Acta*, 2013, **87**, 637-644.
50. L. Cao, M. Lu and H. L. Li, *J. Electrochem. Soc.*, 2005, **152**, A871-A875.
51. M. Al-Ghoul, H. El-Rassy, T. Coradin and T. Mokalled, *J. Cryst. Growth*, 2010, **312**, 856-862.
52. Z. Liu, R. Ma, M. Osada, K. Takada and T. Sasaki, *J. Am. Chem. Soc.*, 2005, **127**, 13869-13874.
53. C. Y. Cao, W. Guo, Z. M. Cui, W. G. Song and W. Cai, *J. Mater. Chem.*, 2011, **21**, 3204-3209.
54. S. L. Wang, L. Q. Qian, H. Xu, G. L. Lu, W. J. Dong and W. H. Tang, *J. Alloys Compd.*, 2009, **476**, 739-743.
55. M. Aghazadehn, M. Hosseinifard, *Ceram. Int.*, 2014, **40**, 3485-3493.
56. M. Rajamathi and P. V. Kamath, *Int. J. Inorg. Mater.*, 2001, **3**, 901-906.
57. J. Jiang, J. Liu, R. Ding, J. Zhu, Y. Li, A. Hu, X. Li and X. Huang, *ACS Appl. Mater. Interfaces*, 2011, **3**, 99-103.
58. H. B. Li, M. H. Yu, X. H. Lu, P. Liu, Y. Liang, J. Xiao, Y. X. Tong and G. W. Yang, *ACS Appl. Mater. Interfaces*, 2014, **6**, 745-749.
59. D. C. Zhang, X. Zhang, X. Z. Sun, H. T. Zhang, C. H. Wang and Y. W. Ma, *Electrochim. Acta*, 2013, **109**, 874-880.
60. C. Mondal, M. Ganguly, P. K. Manna, S. M. Yusuf and T. Pal, *Langmuir*, 2013, **29**, 9179-9187.
61. Z. Hu, L. Mo, X. Feng, J. Shi, Y. Wang and Y. Xie, *Mater. Chem. Phys.*, 2009, **114**, 53-57.
62. X. F. Xia, W. Lei, Q. L. Hao, W. J. Wang, Y. X. Sun and X. Wang, *Electrochim. Acta*, 2013, **113**, 117-126.
63. D. C. Zhang, X. Zhang, Y. Chen, P. Yu, C. H. Wang and Y. W. Ma, *J. Power Sources*, 2011, **196**, 5990-5996.
64. A. A. M. Barmi, M. Aghazadeh, B. Arhami, H. M. Shiri, A. A. Fazl and E. Jangju, *Chem. Phys. Lett.*, 2012, **541**, 65-69.
65. B. E. Conway, *Electrochemical supercapacitors: scientific fundamentals and technological applications*, New York: Kluwer Academic/Plenum, 1999.
66. J. Yan, J. Liu, Z. Fan, T. Wei and L. Zhang, *Carbon*, 2012, **50**, 2179-2188.
67. J. Yan, T. Wei, B. Shao, F. Ma, Z. Fan, M. Zhang, C. Zheng, Y. Shang, W. Qian and F. Wei, *Carbon*, 2010, **48**, 1731-1737.

RSC Advances Accepted Manuscript